

This item is the archived peer-reviewed author-version of:

Quantification by aberration corrected (S)TEM of boundaries formed by symmetry breaking phase transformations

Reference:

Schryvers Dominique, Salje E.K.H., Nishida M., de Backer Annick, Idrissi Hosni, Van Aert Sandra.- Quantification by aberration corrected (S)TEM of boundaries formed by symmetry breaking phase transformations
Ultramicroscopy - ISSN 0304-3991 - 176(2017), p. 194-199
Full text (Publisher's DOI): <https://doi.org/10.1016/J.ULTRAMIC.2016.12.022>
To cite this reference: <https://hdl.handle.net/10067/1496540151162165141>

Quantification by aberration corrected (S)TEM of boundaries formed by symmetry breaking phase transformations

D. Schryvers¹, E.K.H. Salje², M. Nishida³, A. De Backer¹, H. Idrissi^{1,4}, S. Van Aert¹

¹ EMAT, University of Antwerp, Groenenborgerlaan 171, B-2020 Antwerp, Belgium

² Department of Earth Sciences, University of Cambridge, Cambridge CB2 3EQ, UK

³ Department of Engineering Sciences for Electronics and Materials, Faculty of Engineering Sciences, Kyushu University, Kasuga, Fukuoka, 816-8580, Japan

⁴ Institute of Mechanics, Materials and Civil Engineering, Université catholique de Louvain, Place Sainte Barbe, 2, B-1348 Louvain-la-Neuve, Belgium

*Corresponding author: nick.schryvers@uantwerpen.be

Abstract

The present contribution gives a review of recent quantification work of atom displacements, atom site occupations and level of crystallinity in various systems and based on aberration corrected HR(S)TEM images. Depending on the case studied, picometer range precisions for individual distances can be obtained, boundary widths at the unit cell level determined or statistical evolutions of fractions of the ordered areas calculated. In all of these cases, these quantitative measures imply new routes for the applications of the respective materials.

Keywords: aberration correction; quantification; alloys; oxides; phase transformation; pico

Introduction

Crystal defects in materials are well known for their importance for the behavior of the material. From point defects providing the colors in precious stones over moving dislocations dictating the mechanical behavior of metals to precipitates affecting the magnetic properties in alloys, in all cases the defect structures are primordial to the functionality of the material. To understand, predict and possibly tune these parameters it is crucial to understand the exact atomic structures of these defects is essential. Indeed, because of lattice relaxations, when compared with the perfect matrix, small displacements or rearrangements of atoms can be expected at the sites of the defects. Depending on the system, such effects can be seen at the nanoscale, but in some cases they are limited to the picorange or to minor changes in chemical concentration. In this context aberration corrected transmission electron microscopy (AC-TEM) with image resolutions below the Ångstrom and, more importantly, precisions in the picorange, becomes an important tool [Haider et al., 1998; Xu et al., 2005; Bals et al., 2006; Urban, 2008; Jia et al. 2008]. Also, Z-contrast quantification in an AC-TEM can yield information on individual atomic site occupations [Pennycook et al., 1991; Van Aert et al., 2011; Martinez et al., 2014].

In the present work the focus will be on crystallographic boundaries generated by symmetry breaking phase transformations. Four examples of recent work in this field will be reviewed, two on polar oxide systems, CaTiO₃ and LiNbO₃, and two on metals, one with a diffusive (Co-Pt) order-disorder and one with a displacive martensitic (Ni-Ti) phase transformation. In the oxide systems as well as the martensite the aim is to measure local atom displacements

next to the boundary, while for the order-disorder system the focus will be on determining the type and number of atoms in a given column. For more details on some of these examples the reader is referred to the recent literature [Van Aert et al., 2012; Akamine et al., 2015; Gonnissen et al., 2016; Ghidelli et al., 2015].

Experimental

The work was performed with two FEI Titan instruments. The first (Qu-Ant-EM) is equipped with a monochromator and a probe and image aberration correction system allowing scanning as well as conventional TEM imaging to be performed in aberration correction mode. The second (X-Ant-EM) is equipped with a monochromator and probe aberration corrector and focusses on analytical applications. Both instruments also contain an EELS spectrometer while the X-Ant-EM has an in-built ChemiSTEM detector. They both provide direct structural (S)TEM imaging at a sub-Å resolution level which is the focus for the present applications. Both wide beam TEM as well as high angle annular dark field (HAADF) STEM were used. In all cases, statistical parameter estimation was used to quantify the experimental images. In ideal cases, this allows position measurements of all atomic columns with a precision of a few picometers as well as an individual atom counts [A.J. den Dekker et al., 2005, 2013; Van Aert et al., 2009].

Results and discussions

Ferroelastic twin boundary in CaTiO₃

Functional interfaces are not simple structural juxtapositions of the adjacent matrices, but contain novel structural elements which do not exist in the bulk and which may be used as objects in the field of domain boundary engineering. Examples can be superconducting domain boundaries in insulating materials [Aird et al., 1998; Kim et al., 2010], twin boundaries with high defect mobilities [Aird et al., 2000; Seidel et al., 2010; Calleja et al., 2003; Calleja et al., 2001] or a two-dimensional electron gas at interfaces [Ohtomo et al., 2004; Pauli et al., 2011; Huijben et al., 2006; Herranz et al., 2007]. In the present case the focus is on twin boundaries in CaTiO₃ yielding loci of ferroelectricity in a paraelectric matrix. CaTiO₃ single crystals were grown by the floating-zone technique with powders of CaCO₃ and TiO₂ (99.9% purity) as starting materials (Guennou et al., 2010). At room temperature the crystal structure has an orthorhombic Pnma symmetry including micron sized twin variants and twin boundaries resulting from a transformation from the high temperature cubic Pm-3m phase [Goncalves-Ferreira et al., 2008]. The change in lattice parameter is relatively small yielding large twin variants as seen in Fig. 1a, where the inset shows the [001] selected area electron diffraction (SAED) pattern of the product phase in which a small spot splitting of 1.2° of the h-h0 reflection row can be measured. Samples were prepared by conventional Ar⁺ ion milling. The Qu-Ant-EM instrument was used in HRTEM mode at 300 kV followed by reconstructing the exit wave by inverting the image formation process so that all residual lens aberrations are eliminated. To this end the through-focal series reconstruction method was used in which the exit wave is reconstructed from a set of images taken at different defocus values [Coene et al., 1996]. The experimental focal series consisted of 20 images separated by a focal increment of -2.4 nm with the series centered around the zero defocus condition (starting defocus +27 nm) with a spherical aberration constant of +50 μm, a focal spread of 2.9 nm, a convergence angle of 0.15 mrad and a pixel size of 0.0248 nm [Van Aert et al., 2012]. The actual reconstruction of the exit wave was carried out using the TrueImage

software. After reconstruction the residual aberrations were corrected using the standard techniques in TrueImage®.

In Fig. 1b the phase of the reconstructed exit wave of an image containing a twin boundary in CaTiO_3 is shown [Van Aert et al., 2012]. The twin can be recognized by the small orientation difference of 1.2° in the (110) planes and the corresponding spot splitting in the diffraction pattern (inset). This phase part of the exit wave was used for the quantitative analyses since it is directly proportional to the projected electrostatic potential of the structure. The aim is to look for local atom displacements or lattice strain that can induce local ferroelectricity at the boundary. In the rectangular area the atomic positions obtained by the parameter estimation procedure are shown as overlay (Ca = red, Ti = green). From the analysis determining the positions of the different Ca and Ti atomic columns away and close to the twin boundary it is found that shifts in the Ti atomic positions can be measured along and perpendicular to the twin wall. These shifts are shown as arrows in Fig. 1b while the quantitative values are shown in Fig. 2 together with the 90% confidence intervals. Perpendicular to the wall systematic deviations for Ti of 3.1 pm in the second closest layers pointing toward the twin wall are observed. A larger averaged displacement of 6.1 pm is measured parallel to the wall in the layers adjacent to the twin wall. In all layers further away from the twin wall, no systematic deviations are observed. Using the experimental value for the displacement of 6 pm an induced polarization as big as $0.04\text{--}0.2 \text{ C l b m}^{-2}$ is expected. This value is comparable with the bulk spontaneous polarization of BaTiO_3 ($0.24 \text{ C l b m}^{-2}$) and confirms the tendency of interfacial structures to enhance the spontaneous polarization [Neaton et al., 2003]. In other words, by introducing twin walls in this material through a phase transformation, ferroelectricity is generated in a paraelectric matrix. Such twin boundaries can also be introduced by shear rather than by rapid quench and varying the density of these twins can tune the parameters of the material [Van Aert et al., 2013].

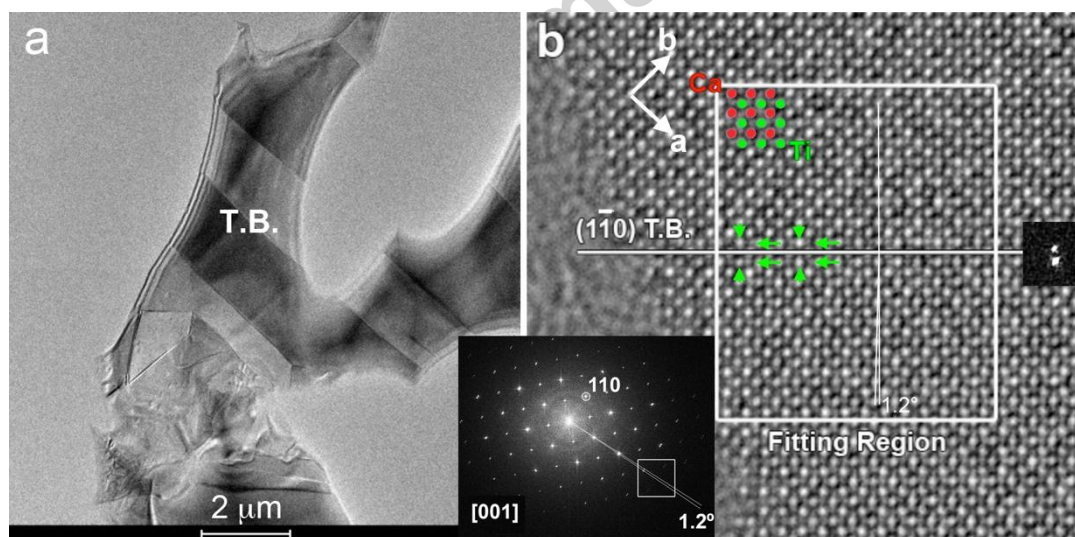


Fig. 1: (a) Micron sized twin boundaries (T.B.) resulting from the cubic to orthorhombic phase transformation in CaTiO_3 with [001] SAED pattern as inset. (b) Phase part of the exit wave obtained by focal series imaging with spot splitting (enlargement from square in SAED inset) seen due to the twinning. The arrows in the rectangle in (b) indicate the directions of measured displacements.

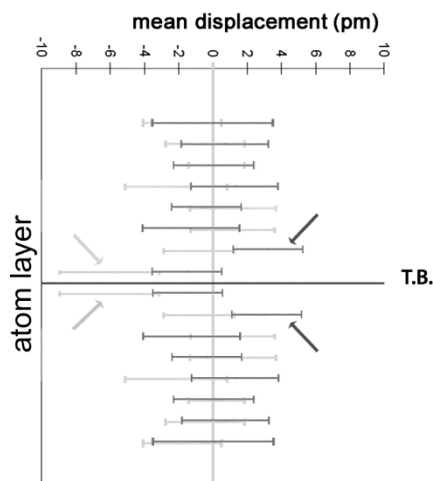


Fig. 2: Measured values for the Ti displacements parallel (light gray) and perpendicular (dark gray) to the interface (T.B.), including 90% confidence intervals. The arrows indicate the first and second atom rows next to the interface showing the measurable displacements.

Ferroelectric domain wall in LiNbO₃

This second example follows the concept of the first one in which a domain boundary provides alternate functionality when compared to the bulk material. Ferroelectric walls in LiNbO₃ are expected to display transport functionality when they are locally electrically charged as a result of an inclination with respect to the equilibrium direction along the ferroelectric polarization direction [M. Schröder et al., 2012; Schröder et al., 2014; Kämpfe et al., 2014; Eliseev et al., 2011]. However, Nataf et al. argued that even “straight” walls should show local inclinations, so that head-to-head and tail-to-tail dipolar kink configurations occur locally [Nataf et al., 2016]. The pattern of atomic displacements at the ferroelectric domain wall in LiNbO₃ was observed using HAADF-STEM. The TEM specimens were prepared using FIB with a dual-beam FEI Helios Nanolab 650 instrument. A double Pt-protection layer and final polishing at low ion-beam energy of 2 kV and current of 23 pA were applied [Gonnissen et al., 2016]. The thickness of the sample was optimized by successive back-and-forth FIB thinning and TEM observation runs and the analyzed region was selected close to the sample surface, i.e., immediately beneath the Pt protection layers where typically the least amount of damage can be expected, as confirmed by the lack of a clear Ga signal in energy dispersive X-ray STEM analysis. FIB lamellae were cut along the [001] crystallographic direction (i.e., normal to the crystal surface) and perpendicular to the domain wall [Myers et al., 1995; Sones et al., 2002; Nataf et al., 2016]. In this orientation, when analyzed with TEM, the samples provide a clear view of the atomic structure along the [1 $\bar{1}$ 0] crystallographic direction, i.e., parallel to the (110) domain wall. HAADF-STEM images were acquired with the Qu-Ant-EM operating at 300 kV as a time series of 49 frames with a very short acquisition time of 2.5 s per frame, a probe convergence semi-angle of 21 mrad, a probe current of 40 pA and the inner angle of the annular detector set at 58 mrad. This mode significantly reduces the dose rate, improving the stability of the material under the electron beam, and minimizes the effect of mechanical instabilities of the sample during the experiment. This stability was confirmed by comparing the results from all 49 frames with those of subsets of this sequence from which it was concluded that no significant changes occurred over the entire series.

Ferroelectric walls in LiNbO_3 are formed at the onset of ferroelectricity near 1483 K at which the paraelectric trigonal structure with $R\bar{3}c$ space group loses its inversion symmetry to become an $R3c$ trigonal structure and separate domains with polarizations pointing in opposite directions (180° walls) are generated. While the bulk is known not to contain any electric charges besides those related to point defects, the walls are locally electrically charged and are expected to display transport functionality. The geometrical condition for charged walls is that they are inclined with respect to the equilibrium direction along the ferroelectric polarization direction $[001]$ [Schröder et al., 2012, 2014; Kämpfe et al., 2014]. However, it can be argued that even ‘straight’ walls can show local kinks so that head-to-head and tail-to-tail dipolar configurations occur locally [Nataf et al., 2016]. Each such configuration represents an increase or decrease of carrier concentrations and are hence local charge monopoles. The aim of this investigation is to investigate the fine structure of the wall and whether or not kinks exist in so-called straight walls and if so, at what scale.

Fig. 3a shows a close up of one of the original HAADF-STEM images in which the (near-to-vertical) wall is located near the center of the image but cannot be recognized by the naked eye. In the present $[1\bar{1}0]$ imaging direction and conditions the Nb columns are seen as white dots. By using parameter estimation theory for determining the x and y positions of each Nb atomic column from the total image averaged over 49 frames, the exact position of the wall can be identified [Gonnissen et al., 2016]. In fig. 3b an example for a small area around the boundary is shown. The up and down pointing arrows indicate the shift of each atomic column in the $[001]$ direction with respect to a reference line defined as the average between the Nb sites on either side of the wall [Gonnissen et al., 2016]. The (red) near-to-vertical full line segments are located at the unit cells over which the direction of this shift changes. From this it is immediately clear that the wall, although macroscopically straight and parallel with the (110) plane, shows kinks at the unit cell scale. A master curve produced by combining all rows further shows an extremely sharp boundary [Gonnissen et al., 2016], with no measurable local strains as for CaTiO_3 . For the investigated length of 90 atomic rows, the wall meanders over about 7 unit cells in width, this width being indicated by the two (purple) near-to-vertical full lines on either side of the wall (their location taking a larger area above and below this selected region into account). In other words, even for equilibrated walls, the wall locally meanders yielding local wall directions inclined with respect to the ferroelectric polarization. These meanders generate kinks and dipolar configurations where the ferroelectric dipoles are created. These configurations necessarily induce local charges, but which do not destabilize the overall wall configuration.

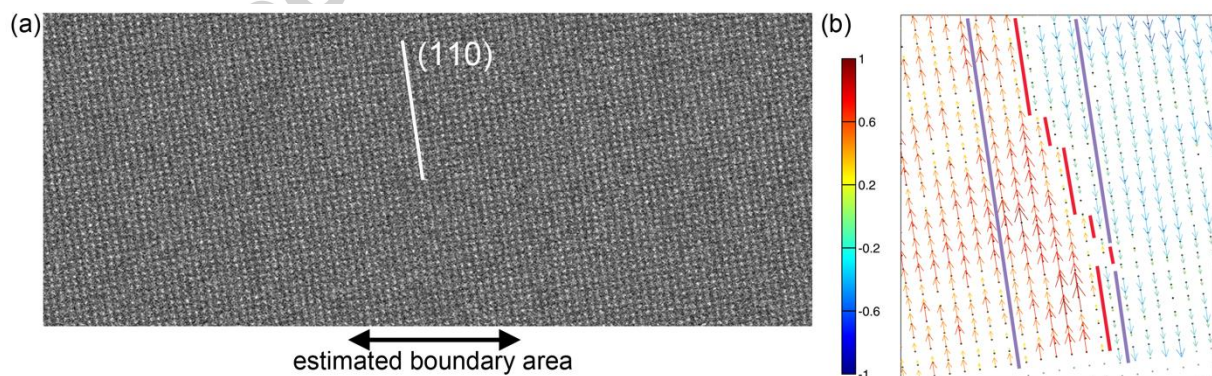


Fig. 3: (a) Single HAADF-STEM image (as part of the 49 frames series) of a ferroelectric wall in LiNbO_3 . (b) Arrows indicating the shifts of the Nb atom columns with respect to the calculated reference position on either side.

One of the important unknown characteristics of anti-phase boundaries (APBs) in ordered magnetic materials is the variation of degree of order near the boundary, where a lower degree of order gives rise to a decrease of magnetic anisotropy thus impacting on any potential applications of the magnetic material [Collins et al., 1963; Ruiz et al., 2005; Lambri et al., 2014]. In order to investigate this degree of order, one variant of the fcc-based $L1_0$ ordered structure in a CoPt alloy, space group $P4/mmm$, was preferentially grown by a dedicated heat-treatment in a magnetic field resulting in several APBs between different domains of the same $L1_0$ variant [Farjami et al., 2008]. After demagnetization by an ensuing magnetic field-free heat-treatment (S)TEM samples are prepared by mechanical polishing, dimpling, and precession Ar^+ ion milling. Aberration corrected HAADF-STEM imaging was carried out with the X-Ant-EM operating at 200 kV with a convergence angle of 21 mrad and the collection of the HAADF detector ranging from 91 to 160 mrad. First and second order aberrations were corrected between each image to compensate for the remaining local magnetic nature of the sample [Akamine et al., 2015].

Fig. 4a shows an HAADF-STEM image including a single APB within the Co-Pt $L1_0$ ordered matrix observed in the $[100]$ zone, i.e., with pure Co and Pt columns parallel with the incident beam and seen as dark and bright columns, resp., in the areas away from the APB. On the left side of the image, the APB shows a curved habit plane while at the top-right corner it becomes parallel with the (001) planes of the present variant. With the displacement vector in the present example being equal to $1/2[011]_{L1_0}$, the character of the APB in this area is non-conservative. More specifically, in the top-right corner the displacement vector is inclined to the boundary and one would expect two adjacent Pt or Co planes for a perfectly sharp APB. In the enlargement of the upper-left inset, atomic columns in the vicinity of the APB exhibit intermediate brightness between pure Co and Pt columns, indicating that these columns are a mixture of Co and Pt along the projection direction. In the lower-right inset, the APB lies along the (001) plane and the width of the region having an intermediate contrast is narrower than on the left side while the intensity of the atomic columns indicates that in the present example the adjacent planes at this non-conservative APB belong to the Pt sublattice.

By using the scaling of the intensities of the atomic columns with the average atomic number of the atoms in the given column [Pennycook et al., 1991] and by using the perfect lattice away from the APB as a reference for the parameter estimation procedure, it is possible to determine the concentration of the atomic columns at and thus the width or inclination of the boundary. For the location where the APB is seen edge-on, i.e., lower-right inset in Fig. 4a, it was found that in the APB contrast area only the two central horizontal planes consist of mixed columns, as seen in Fig. 4b [Akamine et al., 2015]. In this way the system solves the local non-conservative character of the APB. Although the present technique of averaging over several atomic columns in a given row parallel to the boundary does not allow any conclusions on the atom occupation at every individual column, the observation that in the CoPt system the APBs are very narrow does imply these will have no remarkable effect on the net magnetic properties of the material due to their small total volume fraction. The width of the transition zone on the left part was found to be 15 ± 2 atomic columns [Akamine et al., 2015]. Since both areas arise from the same APB it is most likely that the left part is also a sharp APB but tilted with respect to the incident beam direction. In this case, the atomic columns in the transition area must be mixed columns consisting of Co atoms at the bottom and Pt atoms at the top or vice versa. Unfortunately, a distinction between both possibilities could not be made with the present data.

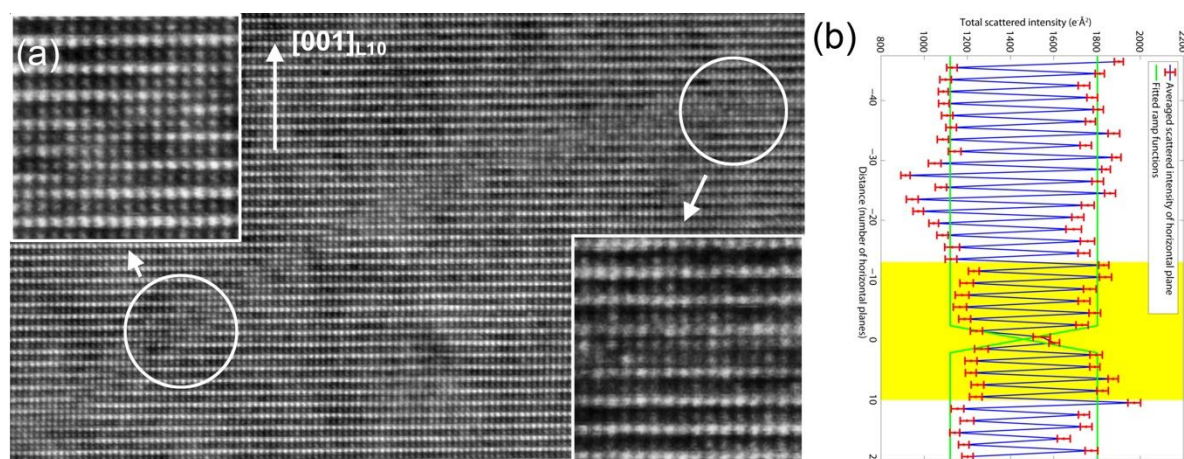


Fig. 4: (a) HAADF-STEM image of a curving non-conservative APB in CoPt. (b) Measurement of the averaged intensities of the planes parallel to the APB viewed edge-on showing a width of 2 planes.

Twin boundary in Ni-Ti B19' martensite

The use of the martensitic transformation in Ni-Ti materials for shape memory and superelastic applications is to a large extent based on the movement of twin boundaries. The local atomic bonding at such boundaries is thus of primordial importance and is linked with the atomic distances across the twin plane. Proper modelling of martensitic transformations and the resulting shape memory and superelastic behavior should take the corresponding twin boundary energies into account, for which accurate atomic positions are needed [Sestak et al., 2011; Ezaz et al., 2011; Zarkevich et al., 2014; Zhong et al., 2014]. Aberration corrected HRTEM at 300 kV was used in an attempt to measure the difference between the interatomic distances in the martensite matrix and across a (11-1) Type I boundary in a Ni₅₀Ti₅₀ B19' martensite, space group P21/m, originating from symmetry breaking of the B2 austenite structure with space group Pm-3m [Nishida et al., 1995, 1995b, 2012, 2012b] and thinned to transparency by electropolishing [Bals et al., 2007].

A typical $\langle 011 \rangle_{B19'}$ zone image of such an boundary is shown in Fig. 5a with the (11-1)_{B19'} planes running nearly vertical. The twin boundary is located near the centre of the image and reveals a slightly darker brightness than the surrounding matrix. For the present imaging conditions, multislice simulations show that the white dots appear in between the atom columns, as shown in the inset of Fig. 5b. As a result, the atomic twin plane belonging to both variants is also located in between two rows of white dots and its location is indicated by double arrows. By using the same approach as the one used for measuring the displacements at the CaTiO₃ boundary a refined parametric model is created and shown in Fig. 5b. From this model image the averaged distances between successive (11-1)_{B19'} rows of white dots are measured, including the 90% confidence intervals corresponding to a precision of around 5 pm. From the data shown in Fig. 5c it can be concluded that the two rows of white dots on either side of the twin plane (double arrows between (a), (b) and (c)) are slightly farther apart (233 pm) than the average distance between two columns in successive (11-1)_{B19'} planes (220 pm) (the latter used as fit with the known lattice parameters of the system). However, also inside the matrix far away from the twin boundary some of the measured distances show a similar deviation (positive as well as negative; single black arrows) so it is at present unclear whether or not the separation is real and affected by the existence of the twin plane.

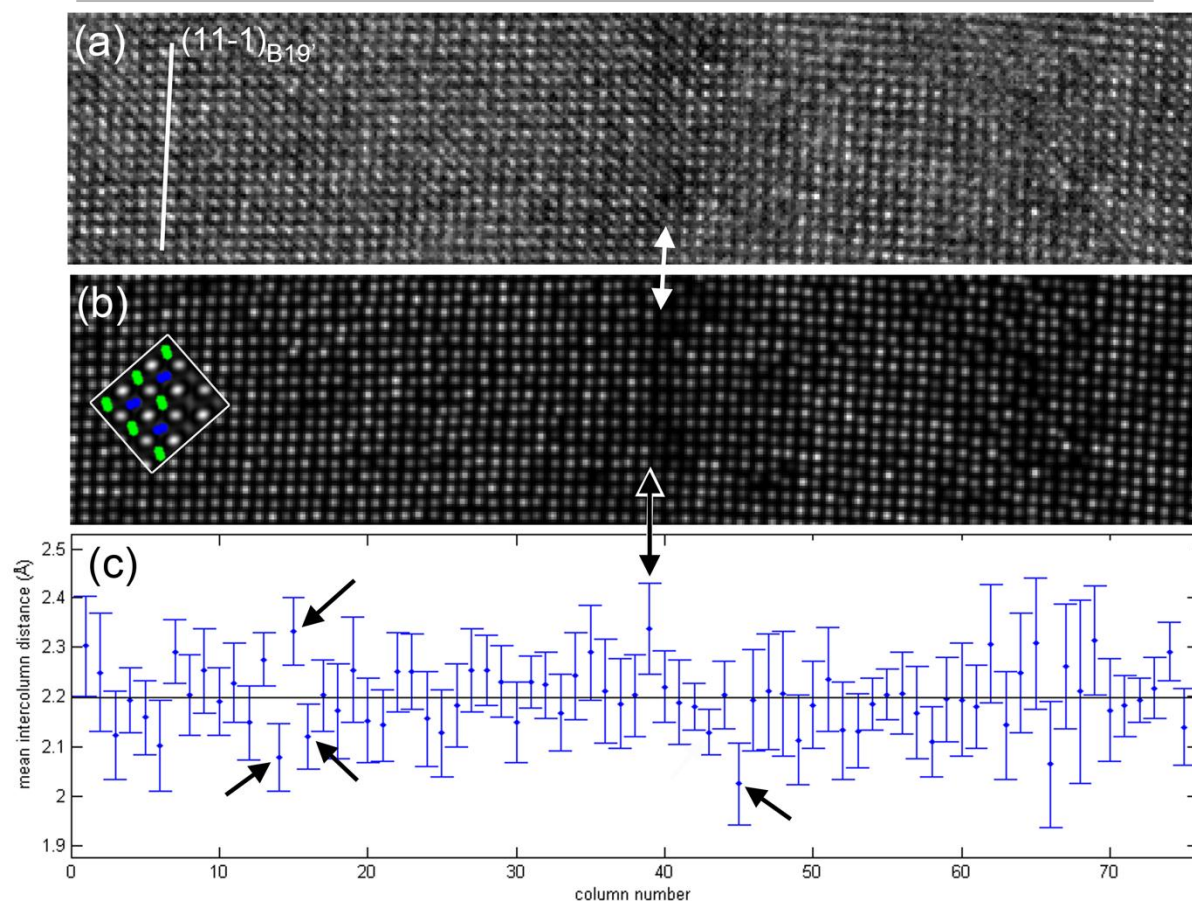


Fig. 5: (a) $[011]_{B19'}$ HRTEM image of a $(11-1)_{B19'}$ Type I twin in Ni-Ti with refined parametric model in (b) and measured intercolumnar distances in (c) with 90% confidence intervals. The inset in (b) shows a magnified simulated image confirming the location of the white dots in between the projected atom columns (Ni = green, Ti = blue).

Conclusions

It is clear from all of the above examples that the quantification, including precision ranges, obtained using various types of aberration corrected electron microscopy, be it at the level of atomic positions or atomic site occupation, has increased our knowledge on the defect structures in various systems. Unfortunately, due to visible variations in the atomic resolution images of the bulk or matrix parts, averaging procedures needed to be used in all cases and conclusions on individual atom columns could not be obtained as yet. Also, the fact that this data has been obtained at the level of individual defects is both a strength and a weakness: averaging over many defects is limited to a minimum, so the overall statistical relevance of the data in view of a macro- or even a microsample should be considered with care. On the other hand, by using proper data treatment approaches, these obtained quantifications will undoubtedly lead to a better understanding and thus routes to new applications of many materials.

Acknowledgments

The authors acknowledge financial support from the Fund for Scientific Research-Flanders (G.0064.10N, G.0393.11N, G.0374.13N, G.0368.15N, G.0369.15N) and the Flemish Hercules 3 program for large infrastructure as well as financial support from the European

Union Seventh Framework Programme (FP7/2007-2013) under Grant agreement no. 312483 (ESTEEM2). EKHS thanks EPSRC (EP/K009702/1) and the Leverhulme trust (EM-2016-004) for support. DS and MN acknowledges financial support from the Japan Society for the Promotion of Science (JSPS, Japan) through the Grant-in-Aid for Scientific Research (A: No. 26249090) and the Strategic Young Researcher Overseas Visits Program for Accelerating Brain Circulation (R2408). HI acknowledges the Belgian Science Policy through the IAP 7/21 project.

References

- Aird A, Salje EKH. *Sheet superconductivity in twin walls: experimental evidence of WO_{3-x}* . J. Phys. Condensed Matter. 1998;10:L377–L380.
- Aird A, Salje EKH. *Enhanced reactivity of domain walls in WO_3 with sodium*. Eur. Phys. J. B. 2000;15:205–210.
- H. Akamine, K.H.W. van den Bos, N. Gauquelin, S. Farjami, S. Van Aert, D. Schryvers, M. Nishida, *Determination of the atomic width of an APB in ordered CoPt using quantified HAADF-STEM*, Journal of Alloys and Compounds 644 (2015) 570–574
- S. Bals, S. Van Aert, G. Van Tendeloo, D. Ávila-Brandé, Phys. Rev. Lett. 2006, 96, 096106.
- Sara Bals, Wim Tirry, Remco Geurts, Zhiqing Yang, and Dominique Schryvers, *High-Quality Sample Preparation by Low kV FIB Thinning for Analytical TEM Measurements*, Microsc. Microanal. 13, 80–86, 2007
- Calleja M, Dove MT, Salje EKH. *Trapping of oxygen vacancies on twin walls of $CaTiO_3$: a computer simulation study*. J. Phys. Condensed Matter. 2003;15:2301–2307.
- Calleja M, Dove MT, Salje EKH. *Anisotropic ionic transport in quartz: the effect of twin boundaries*. J. Phys. Condensed Matter. 2001;13:9445–9454.
- W. M. J. Coene, A. Thust, M. op de Beeck, D. Van Dyck, Ultramicroscopy 1996, 64, 109.
- M F Collins and D A Wheeler, *Magnetic Moments and the Degree of Order in Cobalt-Nickel Alloys*, Proceedings of the Physical Society, 82, 633 (1963)
- A.J. den Dekker, S. Van Aert, A. van den Bos, D. Van Dyck, Ultramicroscopy 2005, 104, 83.
- A.J. den Dekker, J. Gonnissen, A. De Backer, J. Sijbers, S. Van Aert, Ultramicroscopy 2013, 134, 34.
- E. A. Eliseev, A. N. Morozovska, G. S. Svechnikov, V. Gopalan, V. Y. Shur, Phys. Rev. B 2011, 83, 235313.
- T. Ezaz and H. Sehitoglu, *Coupled shear and shuffle modes during twin growth in B2-NiTi*, Applied Physics Letters 98 241906 2011
- S. Farjami, M. Yasui, T. Fukuda, T. Kakeshita, Scr. Mater. 58 (2008) 811.
- M. Ghidelli, S. Gravier, J.-J. Blandin, P. Djemia, F. Momprou, G. Abadias, J.-P. Raskin, T. Pardoen. Acta Materialia 90 (2015) 232
- L. Goncalves-Ferreira, S. A. T. Redfern, E. Artacho, E. Salje, Phys. Rev. Lett. 2008, 101, 097602.
- Julie Gonnissen, Dmitry Batuk, Guillaume F. Nataf, Lewys Jones, Artem M. Abakumov, Sandra Van Aert, Dominique Schryvers, Ekhard K. H. Salje, *Direct Observation of Ferroelectric Domain Walls in $LiNbO_3$: Wall-Meanders, Kinks, and Local Electric Charges*, Advanced Functional Materials (accepted for publication)
- M. Guennou, P. Bouvier, B. Krikler, J. Kreisler, Phys. Rev. B 2010, 82, 134101
- M. Haider, S. Uhlemann, E. Schwan, H. Rose, B. Kabius, K. Urban, Nature 1998, 392, 768.

- Herranz G, Basletic M, Bibes M, Carrétéro C, Tafra E, Jacquet E, Bouzehouane K, Deranlot C, Hamzic A, Broto J-M, Barthélémy A. Fert, *High mobility in LaAlO₃/SrTiO₃ heterostructures: origin, dimensionality, and perspectives*, Phys. Rev. Lett. 2007;98:216803.
- Huijben M, Rijnders G, Blank DHA, Bals S, Van Aert S, Verbeeck J, Van Tendeloo G, Brinkman A, Hilgenkamp H. *Electronically coupled complementary interfaces between perovskite band insulators*. Nat. Mater. 2006;5:556–560.
- H. Idrissi, B. Wang, M.S. Colla, J.P. Raskin, D. Schryvers, T. Pardoën. *Advanced Materials*. 23 (2011) 2119
- C. L. Jia, S.-B. Mi, K. Urban, I. Vrejoiu, M. Alexe, D. Hesse, Nat. Mater. 2008, 7, 57.
- T. Kämpfe, P. Reichenbach, M. Schröder, A. Haußmann, L. M. Eng, T. Woike, E. Soergel, Phys. Rev. B 2014, 89, 035314.
- Kim Y, Alexe M, Salje EKH. *Nanoscale properties of thin twin walls and surface layers in piezoelectric WO_{3-x}*. Appl. Phys. Lett. 2010;96:032904.
- O. A. Lambri, J. I. Pérez-Landazábal, G. J. Cuello, D. Gargicevich, V. Recarte, F. G. Bonifacich, E. D. Giordano and V. Sánchez Alarcos, *Relation between order degree, damping behaviour and magnetic response in Fe-Si and Fe-Al-Si alloys*, Neutron News 25, 2014, 28-31
- G.T. Martinez, A. Rosenauer, A. De Backer, J. Verbeeck, S. Van Aert, *Quantitative composition determination at the atomic level using model-based high-angle annular dark field scanning transmission electron microscopy*, Ultramicroscopy 137 (2014) 12–19
- L. E. Myers, R. C. Eckardt, M. M. Fejer, R. L. Byer, W. R. Bosenberg, J. W. Pierce, *Quasi-phase-matched optical parametric oscillators in bulk periodically poled LiNbO₃*, J. Opt. Soc. Am. B 12, 2102-2116 (1995)
- G. F. Nataf, O. Aktas, T. Granzow, E. K. H. Salje, *Influence of defects and domain walls on dielectric and mechanical resonances in LiNbO₃*, JOURNAL OF PHYSICS-CONDENSED MATTER 28, 015901, 2016
- J. B. Neaton, K. M. Rabe, Appl. Phys. Lett. 2003, 82, 1586.
- M. Nishida, H. Ohgi, I. Itai, A. Chiba, K. Yamauchi, *Electron microscopy studies of twin morphologies in B19' martensite in the Ti-Ni shape memory alloy*, Acta Metallurgica et Materialia, Volume 43, 1995, 1219-1227.
- M. Nishida, K. Yamauchi, I. Itai, H. Ohgi, A. Chiba, *High resolution electron microscopy studies of twin boundary structures in B19' martensite in the Ti-Ni shape memory alloy*, Acta Metallurgica et Materialia, Volume 43, 1995, 1229-1234.
- M. Nishida, T. Nishiura, H. Kawano, T. Inamura, *Self-accommodation of B19' martensite in Ti-Ni shape memory alloys-Part I. Morphological and crystallographic studies of the variant selection rule*, Philosophical Magazine, Volume 92, 2012, 2215-2233.
- M. Nishida, E. Okunishi, T. Nishiura, H. Kawano, T. Inamura, S. Ii, T. Hara, *Self-accommodation of B19' martensite in Ti-Ni shape memory alloys-Part II. Characteristic interface structures between habit plane variants*, Philosophical Magazine, Volume 92, 2012, 2234-2246.
- Ohtomo A, Hwang HY. *A high-mobility electron gas at the LaAlO₃/SrTiO₃ heterointerface*. Nature. 2004;427:423–426.
- Pauli SA, Leake SJ, Delley B, Bjõrck M, Schneider CW, Schlep̃utz CM, Martocchia D, Paetel S, Mannhart J, Willmott PR. *Evolution of the interfacial structure of LaAlO₃ on SrTiO₃*. Phys. Rev. Lett. 2011;106:036101.
- S. Pennycook, D. Jesson, *High-resolution Z-contrast imaging of crystals*, Ultramicroscopy 37 (1991) 14–38.
- Daniel Ruiz, Tanya Ros-Yañez, Leticia Ortega, Laura Sastre, Lode Vandenbossche, Bernard Legendre, Luc Dupré, Robert E. Vandenberghe, and Yvan Houbaert, *Effect of Atomic Order*

- on the Electrical and Magnetic Properties of $Fe_{100-x}Si_x$ ($6 < x < 14$) Alloys*, IEEE TRANSACTIONS ON MAGNETICS, 41, 2005, 3286-3288
- M. Schröder, A. Haußmann, A. Thiessen, E. Soergel, T. Woike, L. M. Eng, Adv. Funct. Mater. 2012, 22, 3936.
- M. Schröder, X. Chen, A. Haußmann, A. Thiessen, J. Poppe, D. A. Bonnell, L. M. Eng, Mater. Res. Express 2014, 1, 035012.
- Seidel J, Maksymovych P, Batra Y, Katan A, Yang S-Y, He Q, Baddorf AP, Kalinin SV, Yang C-H, Yang J-C, Chu Y-H, Salje EKH, Wormeester H, Salmeron M, Ramesh R. *Domain wall conductivity in La-doped $BiFeO_3$* , Phys. Rev. Lett. 2010;105:197603.
- P. Sestak, M. Cerny, J. Pokluda, *Can twinning stabilize B19' structure in NiTi martensite?*, Intermetallics, 19 (2011) 1567–1572
- C. L. Sones, S. Mailis, W. S. Brocklesby, R. W. Eason, and J. R. Owen, J. Mater. Chem. 12, 295 (2002)
- K. W. Urban, Science 2008, 321, 506.
- Sandra Van Aert, Stuart Turner, Rémi Delville, Dominique Schryvers, Gustaaf Van Tendeloo, and Ekhard K. H. Salje, *Direct Observation of Ferrielectricity at Ferroelastic Domain Boundaries in $CaTiO_3$ by Electron Microscopy*, Adv. Mater. 2012, 24, 523–527
- S. Van Aert, J. Verbeeck, R. Erni, S. Bals, M. Luysberg, D. Van Dyck, G. Van Tendeloo, Ultramicroscopy 2009, 109, 1236.
- Van Aert Sandra, Batenburg Joost, Rossell Marta D., Erni Rolf, Van Tendeloo Gustaaf *Three-dimensional atomic imaging of crystalline nanoparticles*, Nature - ISSN 0028-0836 - 470:7334 (2011), p. 374-377
- S. Van Aert, S. Turner, R. Delville, D. Schryvers, G. Van Tendeloo, X. Ding & E. K.H. Salje *Functional twin boundaries*, Phase Transitions: A Multinational Journal, 2013, <http://dx.doi.org/10.1080/01411594.2012.748909>
- X. Xu, S. P. Beckman, P. Specht, E. R. Weber, D. C. Chrzan, R. P. Erni, I. Arslan, N. Browning, A. Bleloch, C. Kisielowski, Phys. Rev. Lett. 2005, 95, 145501.
- N. A. Zarkevich and D. D. Johnson, Shape-memory transformations of NiTi: minimum-energy pathways between austenite, martensites, and kinetically-limited intermediate states, Physical Review Letters 113 (2014) 265701
- Yuan Zhong and Ting Zhu, *Phase-field modeling of martensitic microstructure in NiTi shape memory alloys*, Acta Materialia 75, 2014, Pages 337–347

Highlights

Quantification of

- picometer displacements at ferroelastic twin boundary in $CaTiO_3$
- kinks in meandering ferroelectric domain wall in $LiNbO_3$
- column occupation in anti-phase boundary in Co-Pt
- atom displacements at twin boundary in Ni-Ti B19' martensite